Inorganic Chemistry
Article

*Inorg. Chem.* **2010**, *49*, 8813–8827 **8813**
DOI: 10.1021/ic1015065

# An Aminolytic Approach toward Hierarchical $\beta$-Ni(OH)$_2$ Nanoporous Architectures: A Bimodal Forum for Photocatalytic and Surface-Enhanced Raman Scattering Activity

**Sougata Sarkar,[†] Mukul Pradhan,[†] Arun Kumar Sinha,[†] Mrinmoyee Basu,[†] Yuichi Negishi,[‡] and Tarasankar Pal*,[†]**

[†] *Department of Chemistry, Indian Institute of Technology, Kharagpur 721302, India, and*
[‡] *Tokyo University of Science, 1-3 Kagurazaka, Shinjyuku-ku, Tokyo 162-8601, Japan*

Received May 13, 2010

A surfactantless, trouble-free, and gentle wet chemistry approach has been used to interpret the precisely controlled growth of $\beta$-Ni(OH)$_2$ with the assistance of ammonia and nickel acetate from seedless mild hydrothermal conditions. A thorough investigation of the reaction kinetics and product morphology with varied concentration of NH$_3$ and different reaction times suggests that a putative mechanism of dissolution, recrystallization, and oriented attachment supports the intelligent self-assembly of nanobuilding blocks. Associated characterizations (FTIR, PXRD, FESEM, EDAX, HRTEM, and Raman) have identified it to be pure $\beta$-Ni(OH)$_2$ without any signature of contamination. The assembled units result in porous frameworks (nanoflowers and nanocolumns) and are indeed full of communally intersecting nanopetals/nanoplates with both lengths and widths on the order of micrometer to nanometer length scale. The as-synthesized material could also be used as a precursor for nanometric black NiO under calcination. The hydroxide has been found to be a potent and environmentally benign material because it warrants its photocatalytic activity through dye mineralization. Finally, Ni(OH)$_2$ has been photochemically derivatized with dosages of silver nanoparticles bringing a competent composite authority Ag@Ni(OH)$_2$, to give a full-proof enhanced field effect of prolific SERS activity. In a nutshell, these results are encouraging and fetch new promise for the fabrication of a low-cost and high-yielding greener synthetic protocol for a functional material with promising practicability.

## Introduction

An exponential growth of research efforts have been made to realize systematic control over the size, shape, composition, pattern, and functionality of inorganic nanocrystals owing to their potential and promising applications in diverse areas.[1] Thus, a spectacular variety of inorganic nanocrystals with tailor-made geometries[2] are of profound interest for their subsequent utilization as building blocks for the fabrication of hierarchical nanomaterials with complex architectures to meet different needs. During the last 2 decades, preferentially TiO$_2$, ZnO, Fe$_2$O$_3$, Fe$_3$O$_4$, and CeO$_2$[3] in their nanoregime have been paid more care in the midst of oxide semiconductors because of their structural diversity with innumerable purposeful involvement with other extensively investigated chalcogenide (S$^{2-}$, Se$^{2-}$, and Te$^{2-}$) nanostructures. Now-a-days, owing to their fundamental and technological significance, ever more efforts continue toward "soft" nanocrystal assembly motifs of other transition-metal oxides and hydroxides. Nickel hydroxide [Ni(OH)$_2$], a typical layered double-hydroxide-type material with two well-identified polymorphs ($\alpha$ and $\beta$), is fetching interest for its intended advanced exploitation in electrode materials for high-energy-density batteries, electrochemical supercapacitors, magnetic materials, etc.[4] Ni(OH)$_2$ has also been found to be a suitable solid-state precursor material for metallic nickel as well as NiO.[5] Boosted by these beneficial implementations, an assortment of nanofabrication techniques have been viewed as successful

---

*To whom correspondence should be addressed. E-mail: tpal@chem.iitkgp.ernet.in.

(1) (a) Grätzel, M. *Nature* **2001**, *414*, 338. (b) Rodríguez-Lorenzo, L.; Álvarez-Puebla, R. A.; Pastoriza-Santos, I.; Mazzucco, S.; Stéphan, O.; Kociak, M.; Liz-Marzán, L. M.; Abajo, F. J. G. de *J. Am. Chem. Soc.* **2009**, *131*, 4616. (c) Albrecht, T. A.; Sauvage, F.; Bodenez, V.; Tarascon, J.-M.; Poeppelmeier, K. R. *Chem. Mater.* **2009**, *21*, 3017.

(2) (a) Manna, L.; Scher, E. C.; Alivisatos, A. P. *J. Am. Chem. Soc.* **2000**, *122*, 12700. (b) Zhang, T.; Dong, W.; Keeter-Brewer, M.; Konar, S.; Njabon, R. N.; Tian, Z. R. *J. Am. Chem. Soc.* **2006**, *128*, 10960. (c) Burda, C.; Chen, X.; Narayanan, R.; El-Sayed, M. A. *Chem. Rev.* **2005**, *105*, 1025. (d) Chen, J.; Xiong, Y.; Yin, Y.; Xia, Y. *Small* **2006**, *2*, 1324.

(3) (a) Chen, X.; Mao, S. S. *Chem. Rev.* **2007**, *107*, 2891. (b) Sun, X.; Qlu, X.; Li, L.; Li, G. *Inorg. Chem.* **2008**, *47*, 4146. (c) Laurent, S.; Forge, D.; Port, M.; Roch, A.; Robic, C.; Elst, L. V.; Muller, R. N. *Chem. Rev.* **2008**, *108*, 2064. (d) Yang, S.; Gao, L. *J. Am. Chem. Soc.* **2006**, *128*, 9330. (e) Li, Y.; Liao, H.; Ding, Y.; Fan, Y.; Zhang, Y.; Qian, Y. *Inorg. Chem.* **1999**, *38*, 1382.

(4) (a) Chen, J.; Bradhurst, D. H.; Dou, S. X.; Liu, H. K. *J. Electrochem. Soc.* **1999**, *146*, 3606. (b) Lang, J.-W.; Kong, L.-B.; Wu, W.-J.; Luo, Y.-C.; Kang, L. *Chem. Commun.* **2008**, *44*, 4213. (c) Qi, Y.; Qi, H.; Lu, C.; Yang, Y.; Zhao, Y. *J. Mater. Sci.: Mater. Electron.* **2009**, *20*, 479.

(5) (a) Liang, Z. H.; Zhu, Y. J.; Hu, X. L. *J. Phys. Chem. B* **2004**, *108*, 3488. (b) Wang, Y.; Zhu, Q.; Zhang, H. *Chem. Commun.* **2005**, *41*, 5231.

strategies for the artwork of an unprecedented diverse spectrum of anisotropic $Ni(OH)_2$ superstructures including nanobelts, nano/microtubes, nanorods, microspheres, nanoflowers, nanocarnations, oriented nanocolumns, ribbon- and boardlike nanostructures, and even more.[6] Colloidal synthetic and processing methods have been believed to be flexible enough to allow promising options for large-scale productions of these superlattice assemblies and hierarchical structures and, of course, provide a demanding arsenal over sophisticated equipment-based techniques or rigid experimental conditions. A rational synthetic protocol involving the traditional use of soft and hard templates has been manifested for a rich variety of nanocrystalline materials, although they do present challenges like removal of the templates, etc.[7] In fact, hydrothermal-assisted "one-pot" synthesis has been attempted as a real solution to these challenges and has expanded the arena of achieving the hierarchical frameworks of nanostructures. Also, Ostwald ripening, the Kirkendall effect, dissolution and recrystallization, oriented attachment, etc., are different mechanisms familiarized with this tool for the self-assembly of alleviated three-dimensionally ordered nanostructures. Although the above literature surveys the emergence of new particle anisotropies, there is still the need for a simple, environmentally benign, and less-expensive methodology for the clever organization of anisotropic building blocks to scale-up the rapid development of desired nanostructured materials.

Inorganic nanomaterials with structural porosity therein could lead to a wide variety of promising applications such as gas sensing, and therefore emerging synthetic attempts have been made to induce porosity within the superstructures without any assisting templates.

Herein, entirely simple, cost-effective, completely aqueous solution-based "bottom-up" chemistry has been judged for its implications in the anisotropic assembly through an ammonia-prompted hydrolytic route for controllable syntheses of hierarchical $Ni(OH)_2$ with only the assistance of nickel acetate as the metal ion precursor. A series of reaction parameters, the molar ratio of $Ni^{2+}$ to $NH_3$ and reaction time, upon morphological and crystallographic phase evolution have been synthetically and systematically studied to rationalize the structural configuration. Of course, because $NH_3$ has been employed as a common synthetic reagent for different nanomaterials, the use of soft templates like surfactants as structure-directing agents becomes a necessary tradition. Nonetheless, here only $NH_3$ fuels the fabrication of diverse structural analogues. The surface attachment of $NH_3$ molecules has been authenticated and their spatial participation in hydrogen-bonding interaction has been supposed to regulate the self-templated assembly for microscopic construction with nanometric precision. When the $NH_3$ concentration in the reaction media is tuned, the shape transformation of $Ni(OH)_2$ from porous nanoflowers to hexagonal nanoplates, with the intermediacy of truncated triangular nanoplates, has been achieved, and a probabilistic explanation has been arranged on the basis of the surface energy to explain this fascinating assembly. Stacking interactions between the nanopetals and nanoplates are observed to play a key role in the production of the superstructures, and such assembly-directed crystal engineering to fabricate novel organic/inorganic superstructures has been well reported by Cölfen et al.[8] A quantitative idea of the specific surface area of the porous frameworks has been made with nitrogen adsorption−desorption isotherm studies. A notable finding is the formation of nanoholes caused by dehydration of the hydroxide material during TEM analyses.

Photochemical mineralization of methyl red, an organic dye, has been made under UV irradiation with nanoflower morphology, which substantiates the photoactivated catalytic nature of the semiconductor material, and a comparative account of its catalytic activity has also been manifested, in contrast with nanoporous NiO (derived by annealing $Ni(OH)_2$) and commercial NiO.

Benefitting from the intrinsic porous network, the flower allows the platform to accommodate a secondary material like metal nanoparticles, and this typical characteristic lends a hand to house silver nanoparticles over the nanoframeworks in our effort. The hybrid material has been characterized with proper care and, finally, the state-of-the-art efficiency of the composite material [$Ag@Ni(OH)_2$] lies with their manifestation as a superior surface-enhanced Raman scattering (SERS) substrate for suitable nearby molecules. Analyzing the observed spectroscopic results, we suggest the augmented charge transfer from metal to ligand for the composite when compiled with $Ni(OH)_2$.

Thus, to this end, an attempt has been made successfully to lay out the fabrication of a material with tunable hierarchy with the assistance of molecular linkage, and the material with its parallel bimodal activity, photocatalysis, and SERS characteristics deserves special attention.

## Experimental Section

**Materials.** Nickel acetate [$Ni(OCOCH_3)_2 \cdot H_2O$] and ammonia were purchased from Sisco Research Laboratory, Mumbai, India. Hexamethylenetetramine (HMT/hexamine; $C_6H_{12}N_4$) and pyridine were purchased from Merck, Gurgaon, India. Silver nitrate was purchased from Aldrich. All glassware was cleaned using aqua regia, subsequently rinsed with a copious amount of double-distilled water, and dried well prior to use. Double-distilled water was used throughout the course of the investigation.

**Synthesis.** Nanosized two-dimensional (2D) and three-dimensional (3D) hierarchical $Ni(OH)_2$ nanostructures have been synthesized by adapting amine-assisted hydrolysis of aqueous nickel acetate with the aid of a modified hydrothermal (MHT) protocol.[9a] In a typical preparation of a $\beta$-$Ni(OH)_2$ nanoflower,

---

(6) (a) Dong, L.; Chu, Y.; Sun, W. *Chem.—Eur. J.* **2008**, *14*, 5064. (b) Tao, F.; Guan, M.; Zhou, Y.; Zhang, L.; Xu, Z.; Chen, J. *Cryst. Growth Des.* **2008**, *8*, 2157. (c) Yuan, C.; Zhang, X.; Su, L.; Gao, B.; Shen, L. *J. Mater. Chem.* **2009**, *19*, 5772. (d) Ni, X.; Zhang, Y.; Tian, D.; Zheng, H.; Wang, X. *J. Cryst. Growth* **2007**, *306*, 418. (e) Xu, L.; Ding, Y.-S.; Chen, C.-H.; Zhao, L.; Rimkus, C.; Joesten, R.; Suib, S. L. *Chem. Mater.* **2008**, *20*, 308. (f) Yang, L.-X.; Zhu, Y. J.; Tong, H.; Liang, Z. H.; Wang, W. W. *Cryst. Growth Des.* **2007**, *7*, 2716. (g) Zhu, J.; Gui, Z.; Ding, Y.; Wang, Z.; Hu, Y.; Zou, M. *J. Phys. Chem. C* **2007**, *111*, 5622. (h) Yang, D.; Wang, R.; He, M.; Zhang, J.; Liu, Z. *J. Phys. Chem. B* **2005**, *109*, 7654. (i) Tan, Y.; Srinivasan, S.; Choi, K.-S. *J. Am. Chem. Soc.* **2005**, *127*, 3596. (j) Ni, X.; Zhao, Q.; Zhang, Y.; Song, J.; Zheng, H.; Yang, K. *Solid State Sci.* **2006**, *8*, 1312.

(7) (a) Sau, T. K.; Murphy, C. J. *J. Am. Chem. Soc.* **2004**, *126*, 8648. (b) Jana, N. R.; Gearheart, L.; Murphy, C. J. *J. Phys. Chem. B* **2001**, *105*, 4065. (e) Orikasa, H.; Karoji, J.; Matsui, K.; Kyotani, T. *Dalton Trans.* **2007**, 3757.

(8) (a) Wohlrab, S.; Cölfen, H.; Antonietti, M. *Angew. Chem., Int. Ed.* **2005**, *44*, 4087. (b) Jones, F.; Cölfen, H.; Antonietti, M. *Biomacromolecules* **2000**, *1*, 556. (c) Wohlrab, S.; Pinna, N.; Antonietti, M.; Cölfen, H. *Chem.—Eur. J.* **2005**, *11*, 2903. (d) Yu, S.-H.; Cölfen, H.; Antonietti, M. *J. Phys. Chem. B* **2003**, *107*, 7396. (e) Wang, T.; Cölfen, H.; Antonietti, M. *J. Am. Chem. Soc.* **2005**, *127*, 3246. (f) Cölfen, H.; Antonietti, M. *Angew. Chem., Int. Ed.* **2005**, *44*, 5576.

(9) (a) Sinha, A. K.; Jana, S.; Pande, S.; Sarkar, S.; Pradhan, M.; Basu, M.; Saha, S.; Pal, A.; Pal, T. *CrystEngComm* **2009**, *11*, 1210. (b) Creighton, J. A.; Blatchford, C. G.; Albrecht, M. G. *J. Chem. Soc., Faraday Trans.* **1979**, *75*, 790.

**Table 1.** Reaction Conditions for the Growth of a Couple of $\beta$-$Ni(OH)_2$ Diverse Nanoarchitectures

| entry | vol. of nickel acetate (0.1 M) taken (mL) | final concn of nickel acetate (mM) | vol. of amine ($NH_3$) taken (mL) | final concn of amine (mM) | $[Ni^{2+}]/[NH_3]$ | products' morphology |
|---|---|---|---|---|---|---|
| 1a | 2.9 | 97 | 0.1 | 500 | 0.194 | an unripened basement |
| 1b | 2.7 | 90 | 0.3 | 1500 | 0.06 | porous nanoflower on a discrete and porous basement |
| 1c | 2.5 | 83 | 0.5 | 2500 | 0.03 | stacked triangular nanoplates on a porous basement |
| 1d | 2.3 | 76 | 0.7 | 3500 | 0.022 | regularly stacked quasi-hexagonal nanoplates on a porous basement |
| 1e | 2.0 | 67 | 1.0 | 5000 | 0.013 | stacked perfectly hexagonal nanoplates on a porous basement |

a precursor solution of the nickel ammine complex $[Ni(NH_3)_6^{2+}]$ was prepared by dripping ammonia (0.3 mL) into 2.7 mL of a 0.1 M $Ni(OCOCH_3)_2 \cdot H_2O$ aqueous solution under continuous-stirring conditions (entry 1b). The resulting blue solution was sealed into a 15-mL-capacity screw-capped closed glass vial with a submerged glass slide (1 cm × 0.5 cm), where the upper edge of the slide leveled off exactly with the air−water interface and was subjected to overnight (~12 h) heat treatment using a tungsten bulb (100 W) illumination in a closed wooden box. This results in the subsequent formation of a uniform greenish-white thin film over the slide. The clear supernatant was decanted off, and the slide was courteously rinsed with water and dried in an air oven at 50 °C for 6 h. A greenish pastelike precipitate was also separated out at the bottom from the reaction medium, which was washed thoroughly with water and dried under a vacuum at 50 °C. Table 1 summarizes the variable reaction conditions of the amminolysis experiments conducted for the achievement of a couple of diverse $Ni(OH)_2$ nanoarchitectures.

**Analytical Measurements. UV−Visible Spectroscopy.** Absorption spectra were recorded in a Spectrascan UV 2600 spectrophotometer (Chemito, Mumbai, India), and the solutions were taken in a 1 cm well-stoppered quartz cuvette.

**Fourier Transform Infrared Spectroscopy (FTIR).** FTIR spectral characteristics of samples were collected in KBr pellets in reflectance mode with a Nexus 870 Thermo-Nicolet instrument coupled with a Thermo-Nicolet Continuum FTIR microscope.

**X-ray Diffraction (XRD) Study.** XRD patterns of the different samples were recorded on a Philips PW-1710 X-ray diffractrometer (40 kV, 20 mA) using Cu Kα radiation ($\lambda = 1.5418$ Å) in the $2\theta$ range of 10−90° at a scanning rate of 0.5° $min^{-1}$. The XRD data were analyzed using *JCPDS* software.

**Field-Emission Scanning Electron Microscopy (FESEM).** The morphology of the samples was analyzed by FESEM using a Supra 40 (Carl Zeiss Pvt. Ltd.) microscope at an accelerating voltage of 20 kV. Compositional analysis of the sample was done by an energy-dispersive X-ray microanalyzer (Oxford ISI 300) attached to the scanning electron microscope.

**Transmission Electron Microscopy (TEM).** TEM analysis of the samples was carried out on a Hitachi H-9000 NAR transmission electron microscope, operating at 100 kV. Samples were prepared by sonication of the powders with alcohol and then placement of a drop of solution on a carbon-coated copper grid followed by solvent evaporation in a vacuum.

**Gas Sorption Measurement.** Nitrogen adsorption and desorption measurements were performed at 77 K using a Quantachrome Autosorb Automated Gas Sorption System utilizing Brunauer−Emmett−Teller (BET) calculations for the surface area and Barrett−Joyner−Halenda (BJH) calculations for the pore-size distribution after the samples were degassed in a vacuum overnight.

**Photocatalytic Degradation of Methyl Red.** The photocatalytic degradation of methyl red was performed under an ambient atmosphere in a reactor equipped with water refrigeration and magnetic stirring. An aliquot of 40 mL of an aqueous solution of methyl red ($10^{-4}$ M) was taken separately in three reactors with 10 mg of catalyst [$Ni(OH)_2$ nanoflower or nanoporous NiO or bulk NiO] in each reactor. The system was allowed to stand for 15 min in the dark to equilibrate and then was irradiated under UV light from the top (15 cm from the solution surface). The radiating source was a 15 W Philips medium-pressure mercury lamp ($\lambda = 365$ nm). The degradation kinetics was monitored from time to time with UV−visible spectroscopy.

**Normal Raman Scattering (NRS) and Surface-Enhanced Raman Scattering (SERS) Measurement.** Raman spectra of the samples were obtained with a Renishaw Raman microscope, equipped with a He−Ne laser excitation source emitting at a wavelength of 632.8 nm and a Peltier-cooled (−70 °C) charge-coupled-device camera. A Leica DMLM microscope was attached and fitted with three objectives (5×, 20×, and 50×). For our experiments, the 20× objective was used. The laser power at the sample was 20 mW, and the data acquisition time was 30 s. The holographic grating (1800 grooves $mm^{-1}$) and the slit provided a spectral resolution of 1 $cm^{-1}$.

**Synthesis of a Silver Colloid.** Colloidal silver nanoparticles were synthesized following the ever-addressed Creighton's protocol[9b] by the reduction of silver nitrate (1 mL, 1 mM) with sodium borohydride (3 mL, 2 mM) in ice-cold conditions with vigorous shaking to aid monodispersity.

**Synthesis of a Colloidal Ag@$Ni(OH)_2$ Nanocomposite.** A weighed (0.015 g) amount of the as-prepared powder $Ni(OH)_2$ sample (nanoflower; sample no. 1b; Table 1) was well dispersed in 5 mL of water through sonication followed by the addition of 5 mL of a 50 mM aqueous solution of $AgNO_3$. Reduction of $AgNO_3$ within the $Ni(OH)_2$ matrix was carried out in a manner of photocatalytic reduction under UV-light irradiation. After completion of the reduction, the yellowish-green sol was repetitively washed with water through centrifugation, and finally the composite material was redispersed in 5 mL of water for further use.

**Preparation of Samples for SERS.** A total of 0.5 mL of the as-prepared colloidal silver sol or the composite materials dispersed in water was placed in a small glass vial, into which 0.5 mL of a stock solution of 4-MP (with the desired concentration) was added, and this substrate−probe assembly was incubated overnight to ensure binding of 4-MP on the nanoparticle's surface. A total of 15 $\mu$L of the above suspension was dropped on a microscope slide, and SERS measurements were started as soon as the solvent evaporated.

## Results and Discussion

To realize promising high-performance applications, hierarchical organizations of $Ni(OH)_2$ nanoarchitectures and their composite materials must meet a wide variety of requirements in terms of the particle size, size distribution, shape and morphology, crystallinity, and phase purity. The different solution-phase synthetic routes assembled in the past decade noticeably involve the high-temperature-driven hydro/solvothermal-assisted hydrolysis and condensation of nickel salts for the fabrication of those $Ni(OH)_2$ nanostructures with dimensions ranging from a few tens to several hundreds of nanometers.[6] Owing to the moisture or water

**Scheme 1.** Recommended Aminolysis−Condensation Combined Scheme toward the Stepwise Evolution of $Ni(OH)_2$ Nanoarchitectures from the Crystallites through a Polycondensation Mechanism

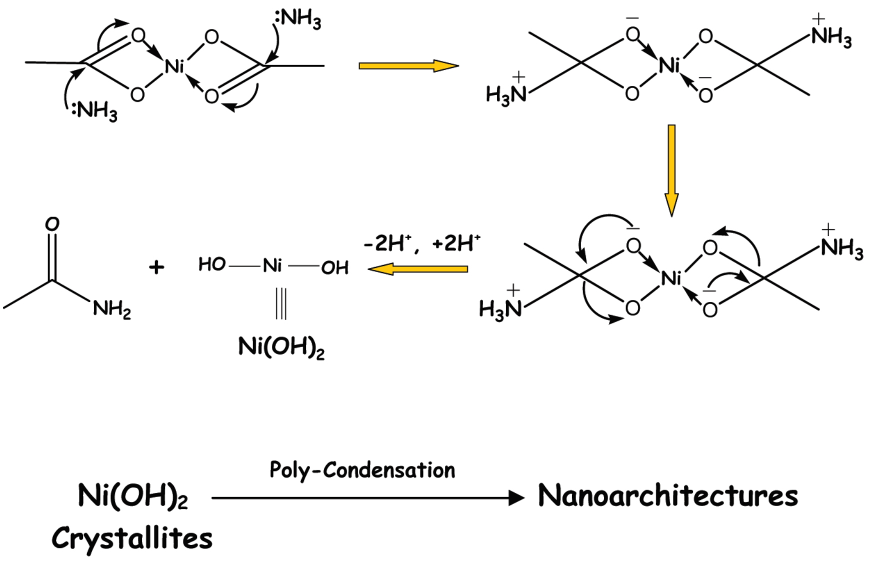

sensitivity, commonly observed for metal salts in most cases, very fast hydrolytic progression at low temperature yields amorphous products with polydispersity and thus high temperature (hydrothermal processing or calcinations) is necessary to bring crystallization.

Therefore, the layout of new preparative protocols could be a suitable alternative to circumventing the existing problems encountered in conventional hydrolytic routes.

The present "aminolytic" challenge ensures the control and tailor making over all of these parameters and properties simultaneously under a one-pot synthetic approach and thus extends the pathway of obtaining hierarchical $Ni(OH)_2$ nanostructures with tunable shape and size.

For the present system discussed here, we have put forwarded a combined aminolysis−condensation mechanism, as illustrated in Scheme 1. In brief, the nucleophilic attack of ammonia onto the electrophilic carboxylate carbon (acetate group) center results in the release of $Ni(OH)_2$ and the formation of an amide. The metal-center-bound hydroxyl groups (an essential requirement for the formation of the Ni−O−Ni bond) then promote the polycondensation reaction with concomitant elimination of water, and the associated outcome is the formation of extensive Ni−O−Ni networks, the key step of crystallization for the nanostructured building block.

Figure 1a illustrates the crystallographic structural characteristics of the as-synthesized samples investigated by XRD analysis. All of the reflection peaks could be indexed entirely to a brucite or C6-type structure (space group: $P3m_1$), with the hexagonal crystal phase of $\beta$-$Ni(OH)_2$ having unit cell of dimensions $a_0 = 3.126$ Å and $c_0 = 4.605$ Å containing one formula unit of $Ni(OH)_2$.[10] These peaks at $d = 4.59$, 2.70, 2.34, 1.75, 1.54, 1.48, 1.35, 1.34, 1.29, and 1.16 Å correspond to the (001), (100), (101), (102), (110), (111), (200), (103), (201), and (202) planes and are in good agreement with the standard values (JCPDS file no. 14-0117), and the broadening of the peaks in the pattern indicates the nanoscale dimensionality of the crystallites. Again this nonuniform broadening of the peaks also advocates that the synthesized material is replete with stacking faults.[11] No obvious peaks from other impurities like $\alpha$-$Ni(OH)_2$ authenticate the high purity of the synthesized product.[12] The representative

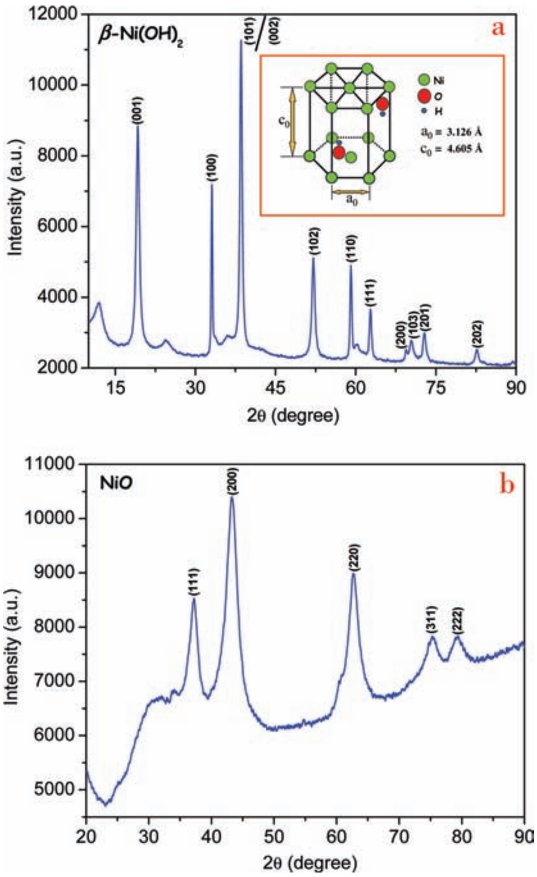

**Figure 1.** XRD pattern of as-synthesized (a) $\beta$-$Ni(OH)_2$ and (b) NiO using Cu K$\alpha$ radiation ($\lambda = 1.5418$ Å).

---

[10] Cai, F.-S.; Zhang, G.-Y.; Chen, J.; Gou, X.-L.; Liu, H.-K.; Dou, S.-X. *Angew. Chem., Int. Ed.* **2004**, *43*, 4212.

[11] Ramesh, T. N.; Kamath, P. V.; Shivakumara, C. *Acta Crystallogr.* **2006**, *B62*, 530.

[12] (a) Jeevanandam, P.; Koltypin, Y.; Gedanken, A. *Nano Lett.* **2001**, *1*, 263. (b) Wang, D.; Song, C.; Hu, Z.; Fu, X. *J. Phys. Chem. B* **2005**, *109*, 1125.

crystal structure presented in Figure 1a (inset in Figure 1a) consists of stacked layers, with each layer having a hexagonal arrangement of nickel atoms with octahedral coordination of the oxygen atoms, and the atoms have the fractional coordinates: nickel 0, 0, 0; oxygen $^1/_3$, $^2/_3$, $z$ and $^2/_3$, $^1/_3$, $\bar{z}$, where $z$ = 0.25.[13] The intrinsic crystal structure possesses an interlayer spacing of 4.605 Å and a Ni·····Ni distance within the layer of 3.12 Å. After being calcined at 350 °C for 4 h in a tube furnace under ambient pressure, the synthesized hydroxide (green) was completely transformed into nickel oxide (NiO, gray-black), explicitly bearing out the well-crystalline nature of the thermally treated product (Figure 1b). The crystalline nature of the calcined sample is well understood owing to the topotactic conversion of the (001) crystallographic plane for $Ni(OH)_2$ to the (111) plane for NiO because cubic NiO affords stacking like that of $Ni^{2+}$ and $O^{2-}$ layers along the (111) direction as does $Ni(OH)_2$ along the (001) direction and also because the $d$ value of the $Ni(OH)_2$ (002) plane agrees well with that of the NiO (111) plane.

FTIR (Figure 2) was employed as an additional probe to evince the presence of major functional groups in $\beta$-$Ni(OH)_2$ (trace a) and annealed $Ni(OH)_2$ for 4 h at 350 °C (trace b). The narrow and sharp band for trace a at ~3645 $cm^{-1}$ is the birthmark for the stretching vibrational mode of non-hydrogen-bonded, geminal, free hydroxyl groups ($\nu_{O-H}$) of the brucite-like sheet structure, while the broad band at ~3437 $cm^{-1}$ for both samples is assigned to the $\nu_{O-H}$ vibration of hydrogen-bonded hydroxyl groups located in the interlamellar space of the samples. This feature presents a clear demonstration of the complete dehydration of surface-adsorbed water molecules in the case of the annealed sample and, in turn, corroborated by the sole presence of the 517 $cm^{-1}$ (in-plane deformation mode of free hydroxyl groups; $\delta_{O-H}$) band only for trace a. Here it is worth mentioning that this 517 $cm^{-1}$ band is exclusive for the $\beta$ phase because this band appears at ~656 $cm^{-1}$ for the α phase.[14] The band at ~1630 $cm^{-1}$ is also ascribed to the bending vibrational mode of surface-adsorbed/trapped (hydrogen-bonded) water molecules. The weak appearance of 1563 and 1405 $cm^{-1}$ bands, indexed to the C=O vibration of the acetate ions ($CH_3COO^-$), accompanied with very weak signatures from 2937 and 2864 $cm^{-1}$ bands ($-CH_2$ vibration), gives foolproof evidence of the presence of trace acetate ions, which are wrapped in the as-synthesized and annealed nanocrystallites and could not be completely washed out. Also, the band discernible at ~666 $cm^{-1}$ is strictly assigned to the bending vibration of the C$-$O species and authenticates the surface attachment of acetate ions once more. The peak at about 1384 $cm^{-1}$ can be ascribed to a $\tau(NH_2)$ twisting vibration individually. Additionally, the basic character of $Ni(OH)_2$ results in the adsorption of atmospheric $CO_2$, and therefore the presence of carbonate anions on their surface could not be avoided, as suggested from the small peak (broad) at ~1384 $cm^{-1}$.[15]

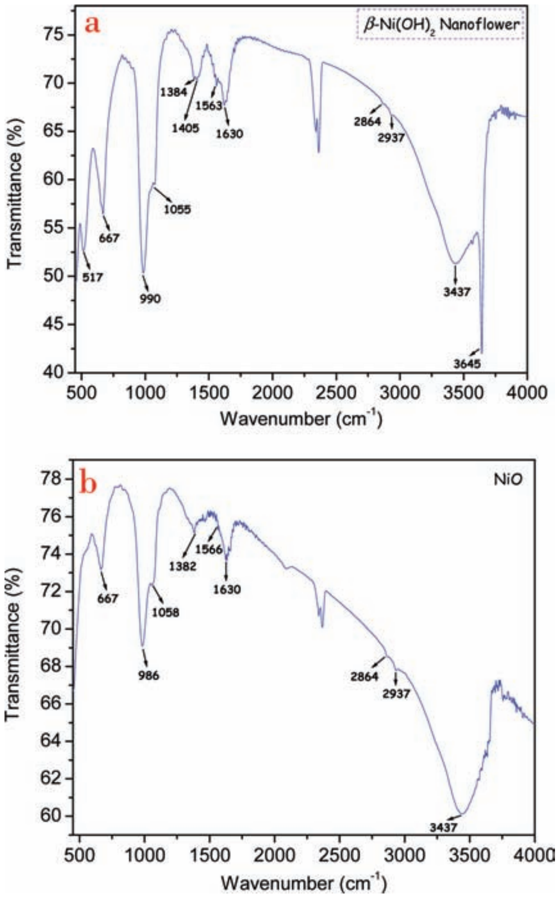

**Figure 2.** FTIR spectrum of (a) the $\beta$-$Ni(OH)_2$ nanoflower and (b) NiO collected in a KBr pellet.

Archetypal SEM images of the synthesized $\beta$-$Ni(OH)_2$ (for entry 1b, Table 1) are shown in Figure 3. The panoramic image in Figure 3a is an overview of the samples with porous flower-mimetic morphology, likely drizzled over a generally fractured and porous pedestal. This SEM micrograph shows that architectures are favorably comprised of densely packed all-but-uniform nanosheets with a thickness of about < 100 nm. The microspherical (diameter ~2 $\mu$m) flowery architecture in Figure 3b is observed to be built up from plentiful patterned and aligned radiating nanopetals with a border length of about 1 $\mu$m. More intriguingly, these petals are interlinked with each other, and a closer inspection of the porous structures reveals the self-assembly-directed oriented attachment of the nanopetals having wavy and rough edges (Figure 3c). A high-magnification SEM micrograph in Figure 3d represents a well-defined and discrete nanoflower having a multilayered and highly ordered texture. The surfaces of the petals are smooth[16] (a probable outcome of Ostwald ripening) and are standing along the radial directions from the center of the microsphere, and they seem to be quite flexible, reflecting their ultrathin feature. The reticulated basement from where the flowers are rooted upwardly is also (Figure 3d) formed by way of interconnecting nanopetals. The entire typical structural aspects of the thin film on the glass slide are again verified with the greenish powder, separated out during synthesis (Figure 3e). The formation of such anisotropic superstructures could be rationalized by a diffusion-limited-aggregation model, where the irreversible aggregation of randomly moving particles results in self-clustering growth and the formation of fractal dimensions.

---

[13] McEwenl, R. S. *J. Phys. Chem.* **1971**, *76*, 1782.

[14] (a) Li, Y.; Xie, X.; Liu, J.; Cai, M.; Rogers, J.; Shen, W. *Chem. Eng. J.* **2008**, *136*, 398. (b) Yang, L.-X.; Zhu, Y.-J.; Tong, H.; Liang, Z.-H.; Li, L.; Zhang, L. *J. Solid State Chem.* **2007**, *180*, 2095.

[15] Freitas, M. B. J. G. *J. Power Sources* **2001**, *93*, 163.

[16] Cheng, Y.; Wang, Y. S.; Zheng, Y. H.; Qin, Y. *J. Phys. Chem. B* **2005**, *109*, 11548.

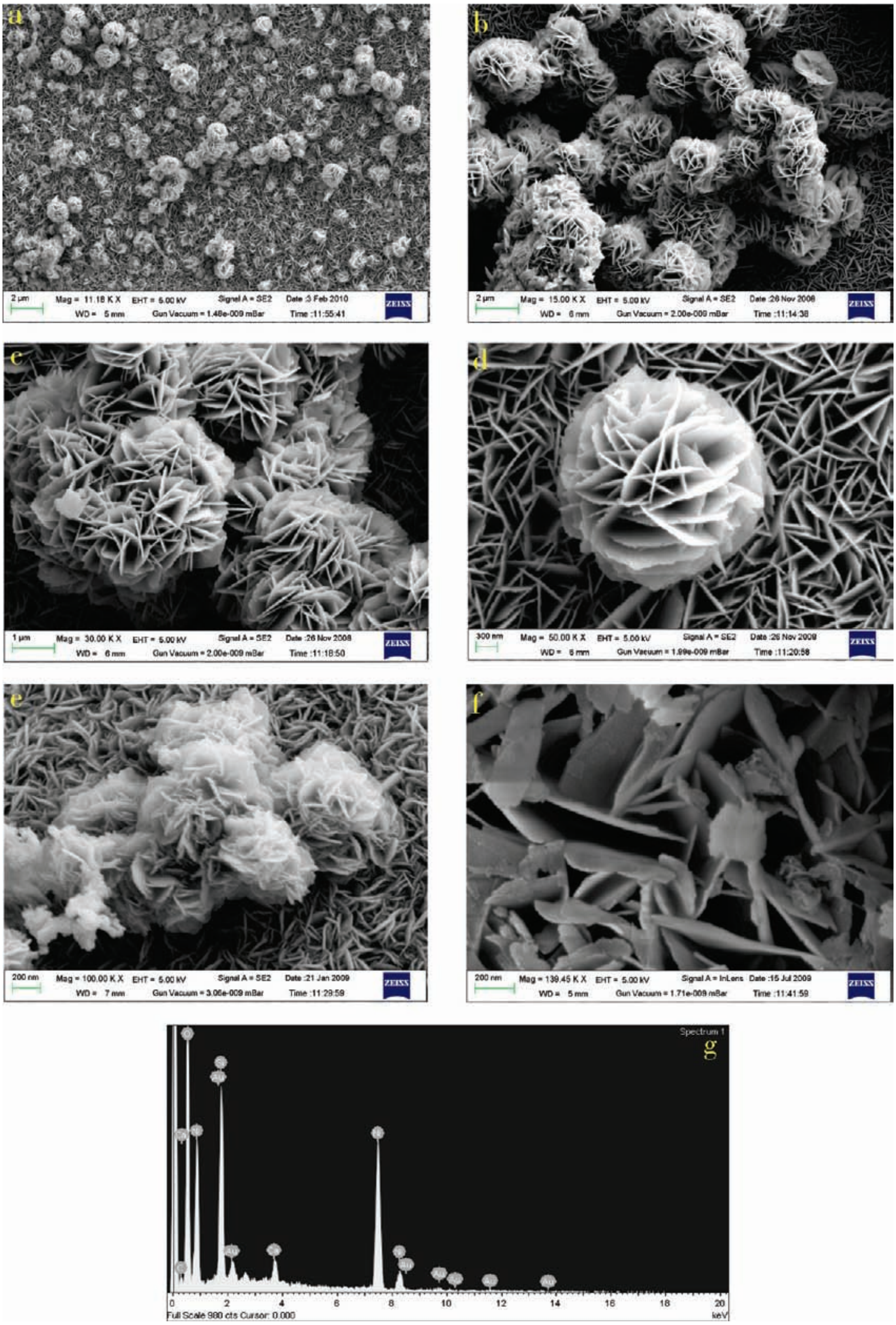

**Figure 3.** Panoramic FESEM images of $\beta$-Ni(OH)$_2$ over glass slides at (a) lower and (b) medium magnifications, (c) an enlarged view of a bunch of nanoflowers made by an oriented attachment of the nanopetals having wavy and rough edges, (d) a well-defined and discrete nanoflower. FESEM images of (e) greenish powder separated out during synthesis [conditions: [Ni$^{2+}$] = 90 mM and [Ni$^{2+}$]/[NH$_3$] = 0.06; MHT overnight (~12 h) using tungsten bulb (100 W) illumination] and (f) gray-black porous NiO obtained after calcination of Ni(OH)$_2$ at 350 °C for 4 h in a tube furnace under ambient pressure. (g) EDX spectrum of the flowery sample.

The porous framework even persists after calcination of the sample (Figure 3f).

Compositional analysis of the sample Ni(OH)$_2$ was achieved with energy-dispersive X-ray (EDX) analysis, revealing that the

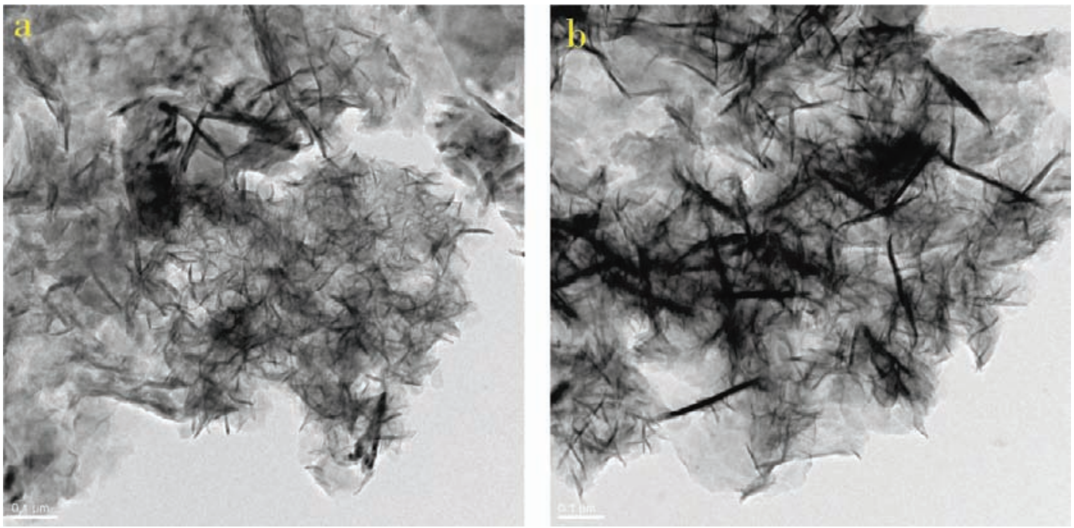

**Figure 4.** Bright-field TEM images of nanoflowers at (a) low and (b) medium magnifications.

coexistence of nickel and oxygen through hydrogen detection was unattainable because the tool could only resolve elements after boron (Figure 3g).[17]

To understand the texture and crystalline orientation of the as-prepared nanostructured sample, further characterization was executed with TEM. Parts a and b of Figure 4 show the low-magnification TEM images of the products after hydrothermal treatment for 12 h, manifesting the formation of flowerlike microstructures abundantly and also revealing that these arrangements are indeed made up of clearly distinguishable nanopetals protruding out from the center having edge-width ranges from 5 to 20 nm. Again, the sharp contrasts among the dark edges of these petals and their faded area underneath unambiguously confirm the well-defined porous structures of the flower and also substantiate the compactness of the petals preferentially in the central region of the flower rather than in the exterior, indicating the density variation of the nanosheets inside the porous architectures. These features associated with the interweaving petal subunits are in good agreement with our FESEM observation. The flowery structures are stable, and no evidence of obvious cracking or destruction into individual nanoplates even under high-intensity ultrasonication could be addressed, signifying that the integrating force between the adjoining nanopetals is the chemical binding at their contacting surfaces as well as feeble van der Waals interactions.[18]

Parts a−d of Figure 5 are typical higher magnification TEM images taken on a piece of extended nanopetal of the flowerlike structures (Figure 5a) at varied magnifications. The identifiable disparity in luminosity in Figure 5b again beefs up the poriferous skeletal subordinate by the interconnected nanopetals of the flowery topology. An enlarged view in Figure 5c clearly discloses that the petals are thin enough. Close inspections of Figure 5d fetch the lattice-resolved HRTEM images of different regional parts surrounded by yellow frames, and the insets therein unequivocally illustrate the (01−10) atomic planes,[5a,6a] with a fringe spacing of 0.27 nm. Keen observation excavates that the synthesized nanostructures are very sensitive to high-energy electron beam irradiation under high-vacuum conditions during TEM sampling and are transformed to porous structures grown with very tiny nanoparticles. As shown in Figure 5e, after being irradiated by an electron beam, copious amounts of holes with distinct atomic planes are generated. In agreement with this, lattice fringes of (111) planes [of $Ni(OH)_2$] can be viewed in HRTEM with a lattice gap of 0.148 nm that corresponds to the separation between the (220) planes of face-centered-cubic NiO. This fascinating feature is a result of dehydration/thermal decomposition of $Ni(OH)_2$ to NiO upon electron beam irradiation, and a literature survey[6a,19] equally highlights this thermodynamically favorable event. Such irradiation can also render electroreduction, as reported by Liu et al., who observed the reduction of $\alpha$-$Ni(OH)_2$ nanosheets to nickel nanoparticles.[20]

Parts a and b of Figure S1 in the Supporting Information are more TEM and HRTEM images taken on different sides of the nanopetals that advocate (i) the promising crystallinity with clearly resolvable interplanar spacing, (ii) the interlocking nanopetals, and (iii) the “electron-beam-issued” porosity once more within the synthesized hierarchies.

The selected-area electron diffraction (SAED) pattern in Figure 5f demonstrates the appearance of periodic diffraction spots, which, in turn, specify the polycrystalline nature of the sample. Interestingly, a few diffraction spots, e.g., at $d$ = 0.874 and 0.78 Å, though these are very weakly intense, also appear with diffraction spots from concentric rings therein, i.e., from (102), (110), and (202) planes. These phenomena have been underpinned in a recent report,[21] where some normally forbidden diffraction spots, such as $^1/_2\{110\}$ and $^1/_2\{102\}$, also appeared besides {110} and {102} diffraction spots. Figure 5g is an emblematical image of the crystal structure, projected along the crystallographic $c$ axis, of $\beta$-$Ni(OH)_2$ crystallizing in the hexagonal system (space group $P3m_1$ and symmetry $D^3{}_{3d}$) common to several halogenides ($CdI_2$ type), with ABAB oxygen packing.[22] The structure can

---

[17] Zhuo, L.; Ge, J.; Cao, L.; Tang, B. *Cryst. Growth Des.* **2009**, *9*, 1.

[18] (a) Liang, J.; Bai, S.; Zhang, Y.; Li, M.; Yu, W.; Qian, Y. *J. Phys. Chem. C* **2007**, *111*, 1113. (b) Mo, M.; Yu, J. C.; Zhang, L. Z.; Li, S. K. A. *Adv. Mater.* **2005**, *17*, 756.

[19] Matsui, K.; Kyotani, T.; Tomita, A. *Adv. Mater.* **2002**, *14*, 1216.

[20] Liu, B.-H.; Yu, S.-H.; Chen, S.-F.; Wu, C.-Y. *J. Phys. Chem. B* **2006**, *110*, 4039.

[21] Li, Y.; Tan, B.; Wu, Y. *Chem. Mater.* **2008**, *20*, 567.

[22] Oliva, P.; Leonardi, J.; Laurent, J. F.; Delmas, C.; Braconnier, J. J.; Figlarz, M.; Fievet, F.; De Guibert, A. *J. Power Sources* **1982**, *8*, 229.

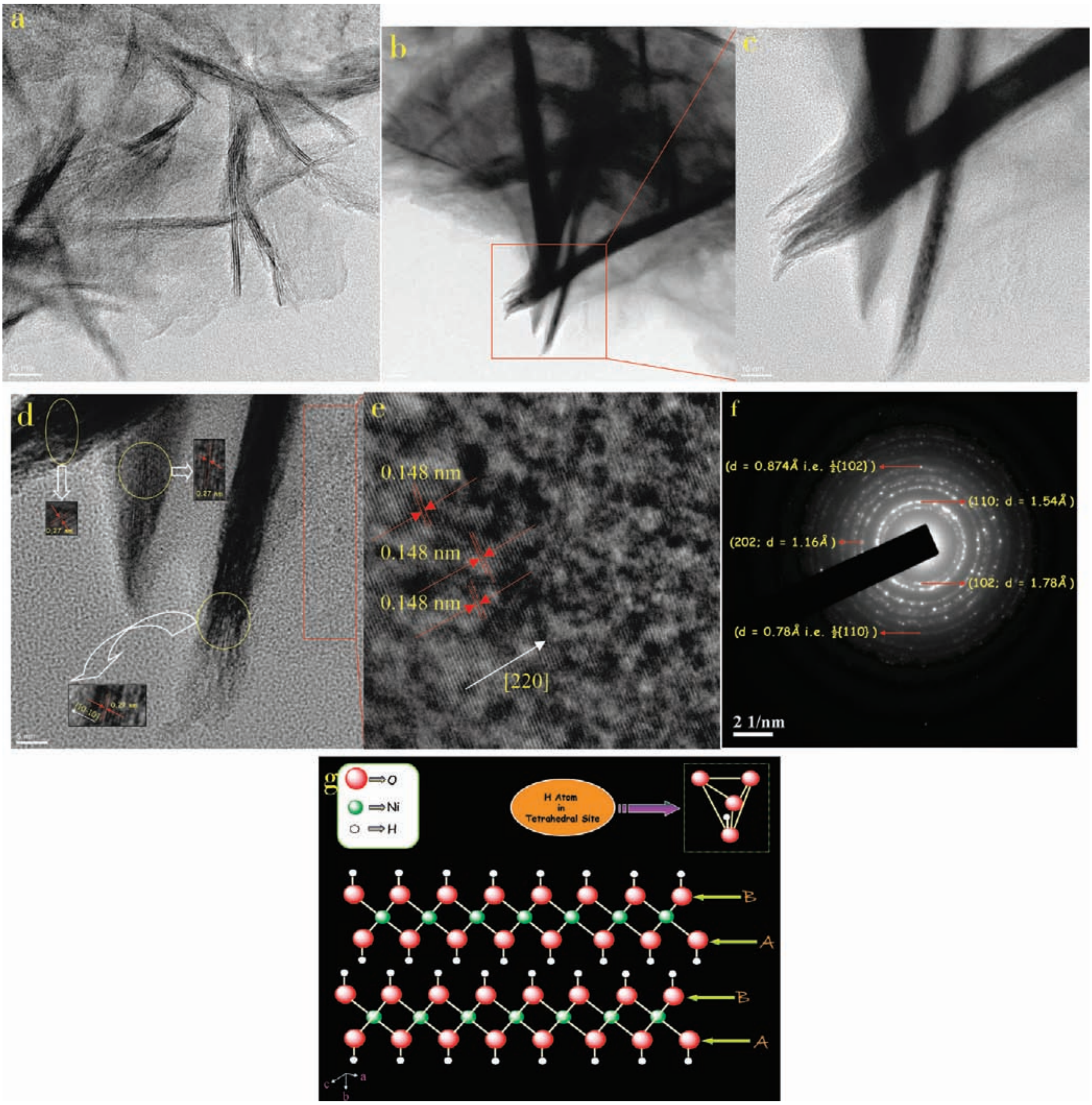

**Figure 5.** HRTEM images of (a) a segment of a nanoflower and (b) intersecting nanopetals, (c) an enlarged view of the enclosed area (marked with red) of part b with a width typically in the range of 5−20 nm and lengths up to several tenths of nanometers. (d) Lattice-resolved HRTEM images of different regional parts (surrounded by the yellow frames) of the nanopetals with a fringe spacing of 0.27 nm and (e) an enlarged view of the enclosed area (marked with a red frame) of part d with copious amounts of holes with a lattice gap of 0.148 nm after being irradiated by an electron beam during high-vacuum TEM sampling conditions. (f) SAED pattern and (g) representative crystal structure of $\beta$-Ni(OH)$_2$.

be visualized as a layered structure, with each layer having an hexagonal planar arrangement of nickel(II) ions with octahedral coordination of oxygen atoms (three lying above the nickel plane and three lying below), and the layers are stacked up along the *c* axis. The hydrogen atoms dwell in the tetrahedral sites, although not perfectly at the central position, of the remaining layers between oxygen atoms and are engaged in tight binding with one of the four oxygen atoms surrounding the tetrahedral sites.

Quantification of the porosity of the flowerlike architectures could be achieved with BET gas sorptometry measurement in view of the nitrogen adsorption/desorption isotherm (Figure 6) and the BJH pore-size distribution (inset in Figure 6). The isotherm can be categorized as type IV with a distinct but narrow hysteresis loop in the relative pressure ($P/P_0$) range 0.2−1.0.[23] Hysteresis at the desorption moment often results from hindered desorption and is observed in particulate samples.[24]

---

(23) Xiong, S.; Yuan, C.; Zhang, X.; Xi, B.; Qian, Y. *Chem.—Eur. J.* **2009**, *15*, 5320.

(24) (a) Wang, Z.; Heising, J. M.; Clearfield, A. *J. Am. Chem. Soc.* **2003**, *125*, 10375. (b) Subbia, A.; Pyle, D.; Rowland, A.; Huang, J.; Narayanan, R. A.; Thiyagarajan, P.; Zon, J.; Clearfield, A. *J. Am. Chem. Soc.* **2005**, *127*, 10826.

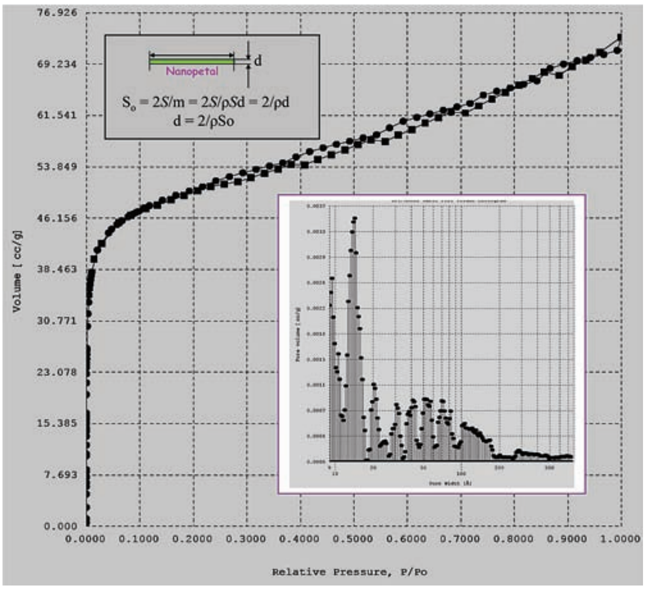

**Figure 6.** Nitrogen adsorption (■) and desorption (●) isotherms of the porous $Ni(OH)_2$ nanoflowers. The insets display the corresponding pore-size distribution plot with a formulaic expression of determination of the average thickness of the nanopetals from a specific surface area ($S_0$) [a distinct but narrow hysteresis loop in the relative pressure ($P/P_0$) range 0.2−1.0; pore-size distribution centered at ~15 Å].

The BET specific surface area is found to be 163.5 $m^2\ g^{-1}$, and the average pore diameter, as calculated from the BJH pore-size distribution plot, addresses the presence of mostly micropores and partly mesopores within the framework with the pore-size distribution centered at ~15 Å. This isothermal result also provides the advantage of obtaining an idea about the average thickness of the nanopetals. A recent report[25] has interpreted the methodology where the specific surface area ($S_0$) could be described as $S_0 = 2S/m$, where $S$ and $m$ are the single surface area and mass of the nanopetals, respectively. Assuming that $\rho$ and $d$ are the mass density and thickness of the petals, we have $S_0 = 2/\rho d$, where $m = \rho Sd$, and this equation provides the average thickness of the nanopetals as 3.08 nm, taking $S_0 = 163.5\ m^2\ g^{-1}$ and $\rho = 3.97\ g\ cm^{-3}$ into account (schematically presented in the inset of Figure 6). The result agrees well with our examined HRTEM images.

Now, a plausible mechanistic interpretation is necessary for an analytical investigation of the reaction mechanism. Initially, the precursor solution (entry 1b) contains $Ni(NH_3)_6^{2+}$ with excess dissolved $NH_3$ (pH ~ 14), and in the ammonia-rich environment, the poorly crystallized nanoparticles are first formed owing to the kinetic advantage through hydrolysis of the hexamine species and result in the formation of solid $Ni(OH)_2$ product (separated from the liquid phase as a powder/thin film) according to the following reaction:

$$Ni(NH_3)_6^{2+}(aq) + 2OH^-(aq) \rightarrow Ni(OH)_2(s) + 6NH_3(aq)$$

After completion of the reaction, pH measurement (observed to be ~10) indicates a decrease in the ammonia concentration through evaporation/solvation with the progression of the reaction, and this value of the pH is close to the "point of zero charge (pzc)" of $Ni(OH)_2$, as was estimated earlier (pzc = 10.7 at 60 °C).[26] Thus, this spontaneous decrease in the pzc value causes favorable self-assembly between the initial tiny nanocrystals in order to reduce the surface energy.[27] Also, it is expected that a series of mononuclear and polynuclear complexes like $NiOH^+$, $Ni(OH)_2$, $Ni(OH)_3^-$, $Ni(OH)_4^{2-}$, $Ni_2OH^{3+}$, $Ni_4(OH)_4^{4+}$, etc., may form in solution in the course of the reaction, and with a change in the solution pH, these species encourage the formation of oligomeric hydroxo moieties through an olation pathway, which elucidates the rapid development of 2D petal-like/platelike building units.[28]

Growth of the nanocrystals in the dynamic reaction environment is typically monitored by the presence of $NH_3$, which controls the hydroxide precipitation along with surface passivation of the nanocrystals, and its responsibility is verified with the products in different time domains (Figure 7) at the standard synthesis conditions. As shown in Figure 7a, at the early stage ($t$ = 4 h), the sample is made up with plentiful but interlocking nanopetals and gives rise to the construction of a porous basement. Eventually, no trace of a nanoflower is observed at this stage. As the reaction proceeds (Figure 7b; $t$ = 6 h), nanoflowers are observed to grow over the microporous platform and retain a hollow interior. The petals are sticking out from the central part of the flower and fewer numbers of petals are engaged in the building of a nanoflower. After 8 h of reaction (Figure 7c; $t$ = 8 h), the growth of the 3D structures happens to be complete, and these are now filled with densely packed nanopetals. We have already described the pattern of the products obtained after 12 h of reaction time, and when the aging time is increased to 24 h (Figure 7d−f; $t$ = 24 h), colonial growth of nanopetals brings forth nanoflowers with more compact architectures. The thicker petals (average thickness ~ 70−100 nm; marked by red arrows) in the structures are grown with self-stacking thin individuals.

Following the whole evaluation process, we are inclined to illustrate the patterning of the $Ni(OH)_2$ textures involving a sequence of dissolution, recrystallization, and oriented attachment.[29] Under hydrothermal conditions, the tiny particles experience a mass relocation by "dissolution and crystallization";[30] the temperature and autogenous pressure increase the solubility of the initially grown fine but amorphous $Ni(OH)_2$ nanoparticles to make a supersaturated growth solution; the process is thermodynamically further driven toward nucleation and crystallization of the tiny nanocrystals with an increase in the reaction time. Moreover, it is a fair assumption that with time the escape of ammonia from the reaction environment trims down its surface passivation effect and the pH of the solution, and when the pH reaches the limit of pzc, spontaneous and quick aggregation between the petals becomes favorable and gives rise to the construction of dense nanostructures.

With a view to obtaining a more comprehensive understanding concerning the role of ammonia, test experiments with varying concentrations of ammonia ($t$ = 12 h) have been performed, and the results are shown in Figure 8. When we have introduced 0.1 mL of $NH_3$ in the reaction system ($[Ni^{2+}]/[NH_3]$ = 0.194; entry 1a of Table 1), neither any

---

(25) Luo, Y.; Duan, G.; Li, G. *J. Solid State Chem.* **2007**, *180*, 2149.

(26) Tewari, P. H.; Campbell, A. B. *J. Colloid Interface Sci.* **1976**, *55*, 531.

(27) (a) Cölfen, H.; Mann, S. *Angew. Chem., Int. Ed.* **2003**, *42*, 2350. (b) Yin, Y.; Alivisatos, A. P. *Nature* **2005**, *437*, 664.

(28) Coudun, C.; Grillon, F.; Hochepied, J.-F. *Colloids Surf., A* **2006**, *280*, 23.

(29) Zhong, L.-S.; Hu, J.-S.; Liang, H.-P.; Cao, A.-M.; Song, W.-G.; Wan, L.-J. *Adv. Mater.* **2006**, *18*, 2426.

(30) Chen, L.-Y.; Zhang, Z.-D. *J. Phys. Chem. C* **2008**, *112*, 18798.

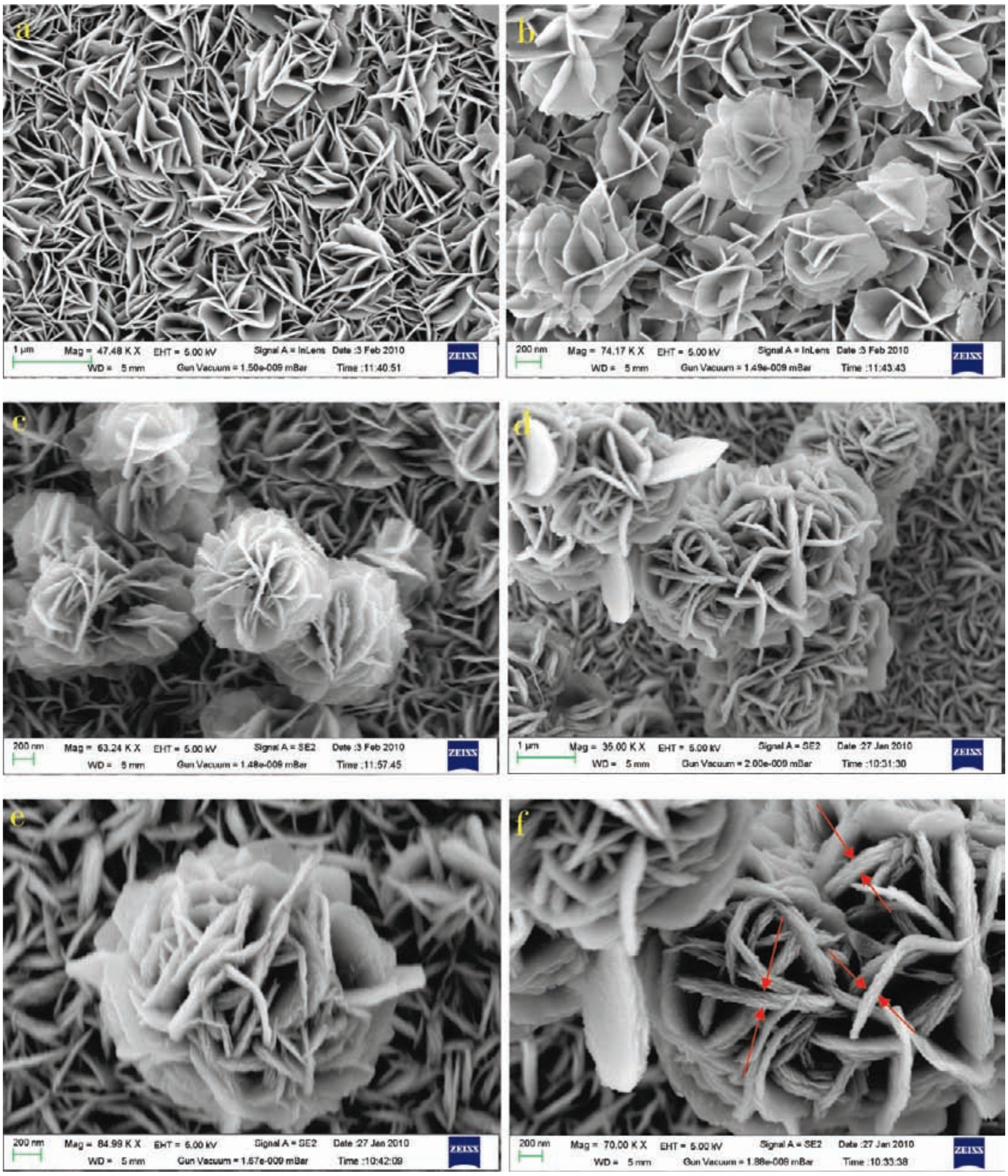

**Figure 7.** FESEM images of synthesized $\beta$-Ni(OH)$_2$ at different reaction time domains: after (a) 4 h (inset gives the impression of "just initialization of budding" of the flowers), (b) 6 h at higher magnification bearing a hollow interior within the nanoflowers, (c) 8 h having full grown nanoflowers fabricated with densely packed nanopetals over a porous platform, and (d−f) 24 h where nanoflowers with more compact architectures are made with thicker but stacked nanopetals [conditions: [Ni$^{2+}$] = 90 mM and [Ni$^{2+}$]/[NH$_3$] = 0.06].

trace of flower nor even well-nurtured nanopetals are observed. The view presents (Figure 8a) only the appearance of an unripened basement made with undergrown nanopetals. Well-defined flowerlike morphology over a discrete and porous basement can only be attained with 0.3 mL of NH$_3$ ([Ni$^{2+}$]/[NH$_3$] = 0.06; entry 1b of Table 1), as was already elaborated on in our previous discussion. A definitive alteration in the product morphology is noted with higher concentrations of NH$_3$. The nanoflowers exit completely from the architectures, and nanoplates enter the framework. Triangular nanoplates (0.5 mL of NH$_3$; [Ni$^{2+}$]/[NH$_3$] = 0.03; entry 1c of Table 1) are seen (Figure 8b) to stick to one another to yield triangular but short-length nanocolumns of length ≥200 to ≤800 nm. An intimate view speaks for the large-scale and uniform productivity of the nanocolumn. Practically all of the triangular faces of the columns (as randomly indicated by red arrows) have an equilateral geometry with side lengths in the range of ~500 nm and all angles measuring 60°. The porous framework of the structure is unveiled from Figure 8c, where we could also observe the covering of the basement with a columnar construction. A similar interlamellar stacking showing growth with "pancake" morphology for $\beta$-Ni(OH)$_2$ was noted in an earlier report.[31] The next approach with 0.7 mL of NH$_3$ ([Ni$^{2+}$]/[NH$_3$] = 0.022; entry 1d of Table 1) could evolute nanoplates again in a cumulated fashion (Figure 8d). Here the nanocolumns seem to result from the regular stacking of quasi-hexagonal nanoplates. The large scalability of the product

---

[31] Coudun, C.; Hochepied, J.-F. *J. Phys. Chem. B* **2005**, *109*, 6069.

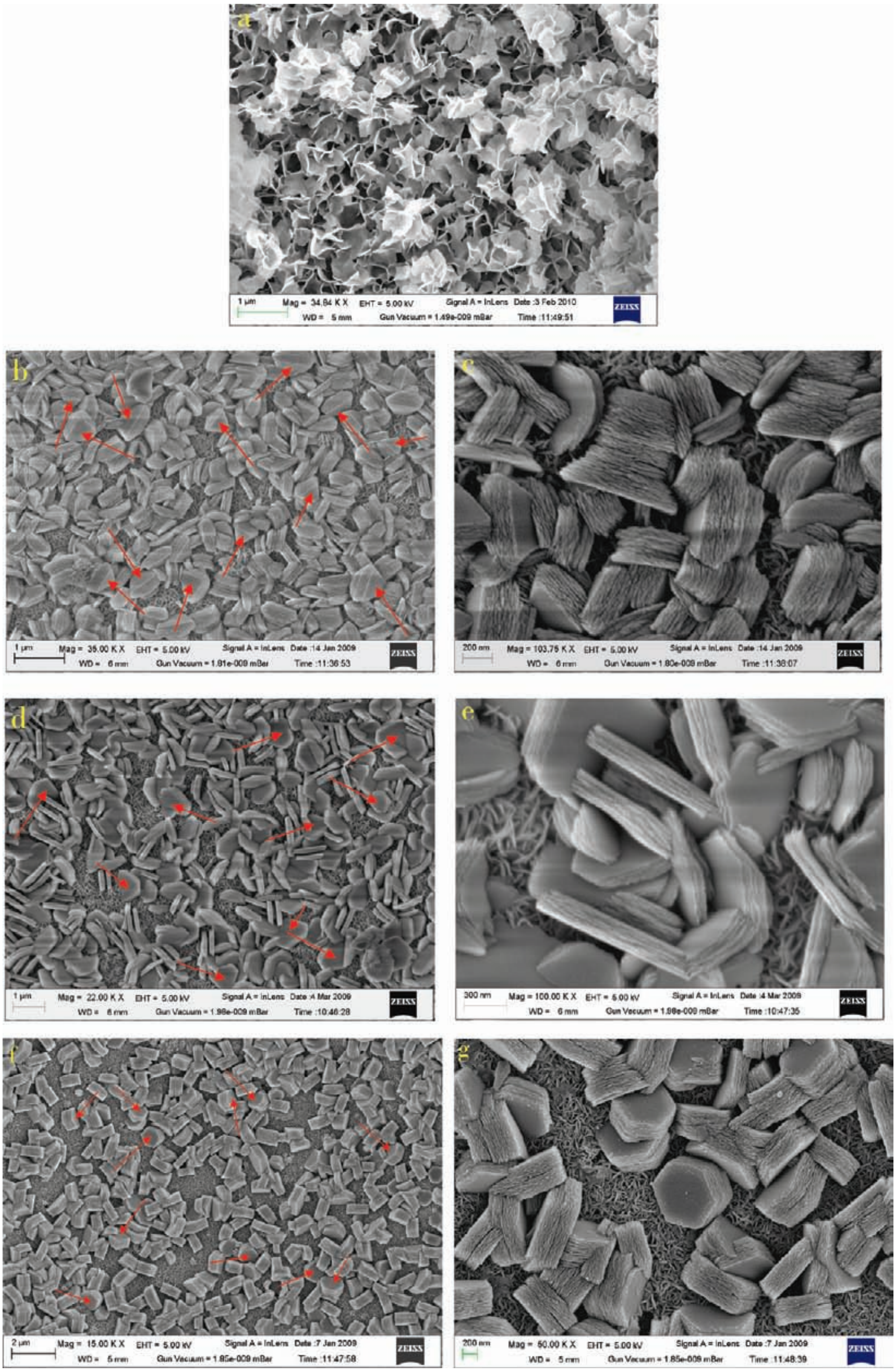

**Figure 8.** FESEM images of as-synthesized $\beta$-$Ni(OH)_2$ products with varying $[Ni^{2+}]/[NH_3]$ ratios: (a) $[Ni^{2+}]/[NH_3] = 0.194$; no nanoflower formation is observed; (b and c) $[Ni^{2+}]/[NH_3] = 0.03$; triangular but short-length nanocolumn built up from stacking triangular nanoplates, their uniform productivity, and porous frameworks; (d and e) $[Ni^{2+}]/[NH_3] = 0.022$; nanocolumns of stacking quasi-hexagonal nanoplates at different magnifications; (f and g) $[Ni^{2+}]/[NH_3] = 0.013$; dozens of nanocolumns with a "honeycomb" outlook cultivated with communally stacking hexagonal nanoplates, where the structures are partly engrossed in the porous basement [conditions: ammonothermal treatment overnight (~12 h) using tungsten bulb (100 W) illumination].

is again demonstrated by this figure, and the enlarged detail (Figure 8e) enables the mean thickness to be estimated as ~200 nm. The faces with truncated triangular geometry (as randomly indicated by red arrows; Figure 8d) stand with discrete edges having a short-arm length of around 500 nm and a long-arm length in the region of ~800 to ~900 nm. When we switch over with the introduction of 1.0 mL of $NH_3$ ($[Ni^{2+}]/[NH_3]$ = 0.013; entry 1e of Table 1) to the nutrient solution to track its effect on the product morphology, we come up with dozens of nanocolumns (Figure 8f) typically hundreds of nanometers in length scale (thickness), thoroughly spread over the porous basement. The "honeycomb" outlook of each of the columns is a consequence of back-to-back stacking interactions among the hexagonal nanoplates (as randomly indicated by red arrows). The face diagonal of a perfect hexagon is estimated to be ~1 $\mu$m, with an internal angle of 120° (Figure 8g). Again, parts of the glued superstructures are observed to be linked with one another in an irregular fashion, accompanied by their partially embedded structural segments within the basement. It is worth mentioning that all of the stacking merely follow an "eclipsed" manner of attachment. The self-assembly route again encourages the columnar micropillars to sustain the porosity within them. TEM images of the hexagonally grown nanocolumns have been displayed in Figure S5 in the Supporting Information, and their subsequent porosity measurement study (Figure S6 in the Supporting Information) has also been elucidated. These statistics thus corroborate the inherent mesoporosity of this assemblage.

Keeping in mind the above information, a qualitative and probabilistic explanation could be recommended to explain the alteration in the hierarchy with a change in the ammonia concentration. The FTIR spectra of the flower (Figure 2a) and hexagonal nanocolumn (Figure S7 in the Supporting Information) show the presence of vibrational bands at ~990 and ~1055 $cm^{-1}$, which arise from the deformation modes of hydrogen-bonded ammonia molecules,[32] and these are accompanied again by the N−H stretching modes in the region of ~3300−3400 $cm^{-1}$ (broad feature). These spectroscopic features indicate the retention of ammonia molecules on the surface of the hydroxides, where the surface passivation of the nanocrystallites may occur in different ways: (i) through hydrogen bonding involving its hydrogen atom to the oxygen atom of surface-anchored hydroxyl groups; (ii) through hydrogen bonding by way of its nitrogen atom with the hydrogen atom of surface hydroxyl groups; (iii) through coordinative interactions with surface metal ions (coordinatively unsaturated). Now, a higher $NH_3$ concentration results in adequate surface coverage, and then they happen to be more prone to engaging in a sufficient amount of hydrogen bonding, which perhaps facilitates the stitching up of the surfaces with each other to cause a more compact architecture. A recent study[33] on the self-assembly tuned growth of $\beta$-$Ni(OH)_2$ single crystals with concave polyhedron structures has described the cross-linking role of hydrazine cleverly introduced into a reaction system in which also the existence of (N−H····O) hydrogen bonding was supported from experimental results. Moreover, the broad band at ~550 $cm^{-1}$ ($\nu_{Ni-N}$; Figure S7 in the Supporting Information) for the hexagonal nanocolumnar structure confirms the superior coverage of their surface with $NH_3$ beyond a doubt.

**Scheme 2.** Schematic Presentation of the Shape Transformation of a Triangular to a Hexagonal $Ni(OH)_2$ Nanocolumn through Truncated Triangular/Quasi-Hexagonal Nanocolumnar Intermediate

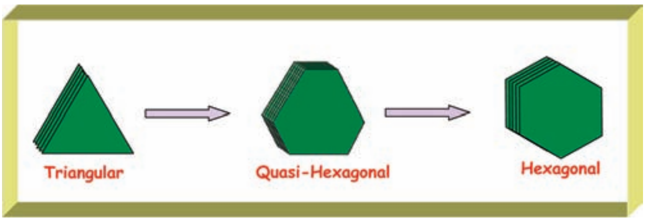

Of definite significance is the distinctively observed ammonia-assisted shape transformation of triangular nanocolumns to hexagonal ones through truncated triangular intermediates (pictorially represented in Scheme 2). Earlier reports have highlighted the phenomenon for metal nanocrystals,[34] and a recent study[35] has reported the transformation from triangular to hexagonal r-BN nanoplates through a simple thermal treatment. Following these literature results, we can come up with a qualitative explanation that suggests the following: for a hexagonal crystal lattice, stable (lowest surface energy) cleavage planes are known to be (10−10) and (01−10) atomic planes with angles of 120°, and therefore the triangular nanoplates, bearing a high surface energy at their tips, thermodynamically transform into the hexagonal ones through the intermediacy of truncated triangular/quasi-hexagonal nanostructures in order to lower the energy. The hexagonal crystal system with four crystallographic axes, three equatorial axes at 120°, and one vertical (c) axis that is perpendicular to the other three withstands the growth direction of the nanocrystals during shape transformation, although in a real state of affairs, this might be more complicated.

Of particular interest, the introduction of $N_2H_4$ as a bidentate linker molecule to pile up $Ni(OH)_2$ nanoplates to achieve columnar packing and the manipulation of the column length are described with a concentration variation of $N_2H_4$.[33] To realize the unique role of $N_2H_4$, they introduced $NH_3$ in lieu of $N_2H_4$, but only flowerlike structures composed of randomly stuck nanoplates resulted. They have addressed their finding with a justification of the molecular structure of $N_2H_4$ and $NH_3$: because a $N_2H_4$ molecule has two nitrogen atoms, layers of nickel hydroxide can be assembled, engrossing its bridging action. However, the $NH_3$ molecule with only one nitrogen atom cannot serve the bridging function and, consequently, the nickel hydroxide layers mount up randomly to give only a flowerlike structure.

Again, another recent report[36] has described the crucial and essential role of an anionic surfactant in getting the microspherical hierarchy of $\beta$-$Ni(OH)_2$ congregated with nanoplates from the $Ni(NH_3)_6^{2+}$ precursor under hydrothermal conditions (120 °C, 12 h), and the key point to be

---

[32] Tsyganenko, A. A.; Pozdnyakov, D. V.; Filimonov, V. N. *J. Mol. Struct*. **1975**, *29*, 299.

[33] Zhou, W.; Yao, M.; Guo, L.; Li, Y.; Li, J.; Yang, S. *J. Am. Chem. Soc*. **2009**, *131*, 2959.

[34] (a) Wang, Z. L.; Petroski, J. M.; Green, T. C.; El-Sayed, M. A. *J. Phys. Chem. B* **1998**, *102*, 6145. (b) Chou, N. H.; Schaak, R. E. *J. Am. Chem. Soc*. **2007**, *129*, 7339. (c) Métraux, G. S.; Cao, Y. C.; Jin, R.; Mirkin, C. A. *Nano Lett*. **2003**, *3*, 519. (d) Jin, R.; Cao, Y. C.; Hao, E.; Métraux, G. S.; Schatz, G. C.; Mirkin, C. A. *Nature* **2003**, *425*, 487.

[35] Li, M.; Xu, L.; Sun, C.; Ju, Z.; Qian, Y. *J. Mater. Chem*. **2009**, *19*, 8086.

[36] Kuang, D.-B.; Lei, B.-X.; Pan, Y.-P.; Yu, X.-Y.; Su, C.-Y. *J. Phys. Chem. C* **2009**, *113*, 5508.

addressed here is the formation of no obvious hierarchy under the same experimental conditions but without any surfactant.

However, to the best of authors' knowledge, this is the first report on the columnar growth (triangular, quasi-hexagonal, and hexagonal) of $\beta$-Ni(OH)$_2$ with a regular stacking of nanoplates with the assistance of only $NH_3$. It has been established that explicit regulation in the structural arrangements of the hydroxide material (from flower to different nanocolumnar structures) meets the need for a simple manipulation in the ammonia concentration. No special and selective assistance (for instance, the presence of a bridging ligand with two successive donor sites like $N_2H_4$ and any structure-directing agent like surfactant) is needed to dish up the purpose.

We have judiciously introduced HMT and pyridine (no N−H bonds) separately in lieu of ammonia to judge their effect on the growth pattern. No obvious formations of well-patterned flower as well as platelike/columnarlike morphologies are observed (Figure S8 in the Supporting Information). This result supports the essential requirement of N−H bond(s) within the structural backbone of added hydrolyzing amine/base for making such 3D superstructures.

Semiconductor-driven photocatalysis, a promising tool for implementing the large-scale purification of wastewaters through extensive mineralization of a variety of environmental pollutants, has received a considerable challenge among the advanced oxidation process. However, the efficiency depends upon their higher crystallinity to minimize electron−hole pair loss owing to the trapping of charge carriers at the defect sites.[37] Although $TiO_2$, ZnO, and $Fe_3O_4$ have been appreciated as esteemed photoactive catalysts,[38] small endeavors have been made to date to explore that possibility with the oxide materials of nickel.[39] Benefitting from the chemical stability of the synthesized hydroxide materials in an aqueous solution even in a strong alkaline medium[20] and the nonphotocorrosivity, we have employed the material (nanoflower) to photocatalyze the degradation of methyl red (MR; color changes from red to yellow) under UV irradiation as a model compound, and a comparative account of its catalytic activity has also been manifested, in contrast with nanoporous NiO [derived from annealing Ni(OH)$_2$] and bulk NiO. Nearly complete degradation (92.5% with nanoflower and 94.03% with nanoporous NiO) becomes possible with the nanophase materials, but the contribution from bulk NiO is only 48.4% even after a long UV exposure time. This enhanced activity of the synthesized materials over the commercial NiO believably results from their high surface-to-volume ratio in the nanostage and porous frameworks. The porosity significantly promotes the photocatalytic activity by allowing multiple reflections of UV light within the internal cavity and also provides immediate contact of the dye molecules through their efficient transport to the interior void.[40] It is expected that, being a p-type wide-band-gap semiconductor with a distorted rock salt structure and the most stable (100) plane, nanometric NiO could be promising in a wide variety of optical properties, and this may well explain the small variance in the efficiency in relation to the hydroxide homologue, as observed in our case. The photodegradation kinetics is followed with UV−visible spectroscopy and is represented in Figure 9a−c, where we can observe the time-dependent change in its absorption profile that corresponds with a steady decrease in $\lambda_{\max}$ (~525 nm) of MR with the concomitant enhancement of a new and broad peak centered at ~425 nm. The fate of $\beta$-Ni(OH)$_2$ upon adsorption of the dye is noticed and is given in Figure 9a. Nonetheless, the dye alone (without catalyst) shows no trace of degradation under identical conditions, and degradation is only achieved with the hydroxide and oxide nanocatalysts within the experimental time scale. A detail representation regarding possible degradation products was mentioned earlier.[38b] Under the experimental conditions, the degradation pathways follow first-order reaction kinetics (Figure 9d) where the rate dependency could be well expressed by the Langmuir−Hinshelwood kinetic model.[41] In the model, the reaction rate ($R$) is proportional to the surface coverage ($\theta$) of the heterogeneous nanomaterials as expressed below:

$$R = -\mathrm{d}C/\mathrm{d}t = k_r\theta = k_rKC/(1+KC)$$

where $C$, $k_r$, and $K$ denote the reaction rate constant, adsorption coefficient of the reactant, and reactant concentration, respectively. With a very low concentration ($C$) of the reactant, $KC$ becomes small enough so that the denominator reduces to 1 and the equation thus describes just first-order kinetics. Assuming $C = C_0$ at $t = 0$ (the start of irradiation), integration of the above equation results:

$$\text{-}\ln(C/C_0) = k'\mathrm{t}$$

where $k'$ is the apparent first-order rate constant evaluated as $1.35 \times 10^{-2}$, $2.03 \times 10^{-2}$, and $8.15 \times 10^{-4}$ min$^{-1}$ for Ni(OH)$_2$ nanoflowers, nanoporous NiO, and bulk NiO, respectively. The well-accepted mechanism for the photocatalytic reaction engrosses photoexcited electron transfer[3a] from the valence band to the conduction band of the semiconductor under consideration, able to initiate the oxidation/reduction processes of a surface-adsorbed substrate. In aqueous solutions, the holes in the valence band are scavenged by surface hydroxyl groups, generating a strong oxidizing hydroxyl radical, which can promote the oxidation and subsequent mineralization of the dye molecule.

While SERS has enjoyed varied applications to in situ interfacial chemistry mostly with "free-electron-like" metals,

---

(37) Hoffmann, M. R.; Martin, S. T.; Choi, W.; Bahnemann, D. W. *Chem. Rev.* **1995**, *95*, 69.

(38) (a) Comparelli, R.; Fanizza, E.; Curri, M. L.; Cozzoli, P. D.; Mascolo, G.; Passino, R.; Agostiano, A. *Appl. Catal., B* **2005**, *55*, 81. (b) Comparelli, R.; Fanizza, E.; Curri, M. L.; Cozzoli, P. D.; Mascolo, G.; Agostiano, A. *Appl. Catal., B* **2005**, *60*, 1. (c) Basu, M.; Sinha, A. K.; Sarkar, S.; Pradhan, M.; Yusuf, S. M.; Negishi, Y.; Pal, T. *Langmuir* **2010**, *26*, 5836. (d) Zheng, Y.; Zheng, L.; Zhan, Y.; Lin, X.; Zheng, Q.; Wei, K. *Inorg. Chem.* **2007**, *46*, 6980. (e) Liu, X.; Fang, Z.; Zhang, X.; Zhang, W.; Wei, X.; Geng, B. *Cryst. Growth Des.* **2009**, *9*, 197.

(39) (a) Song, X.; Gao, L. *J. Phys. Chem. C* **2008**, *112*, 15299. (b) Song, X.; Gao, L. *J. Am. Ceram. Soc.* **2008**, *91*, 4105.

(40) Li, H. X.; Bian, Z. F.; Zhu, J.; Zhang, D. Q.; Li, G. S.; Huo, Y. N.; Li, H.; Lu, Y. F. *J. Am. Chem. Soc.* **2007**, *129*, 8406.

(41) (a) Sun, Z.; Chen, Y.; Ke, Q.; Yang, Y.; Yuan, J. *J. Photochem. Photobiol., A* **2002**, *149*, 169. (b) Sahoo, C.; Gupta, A. K.; Pal, A. *Desalination* **2005**, *181*, 91.

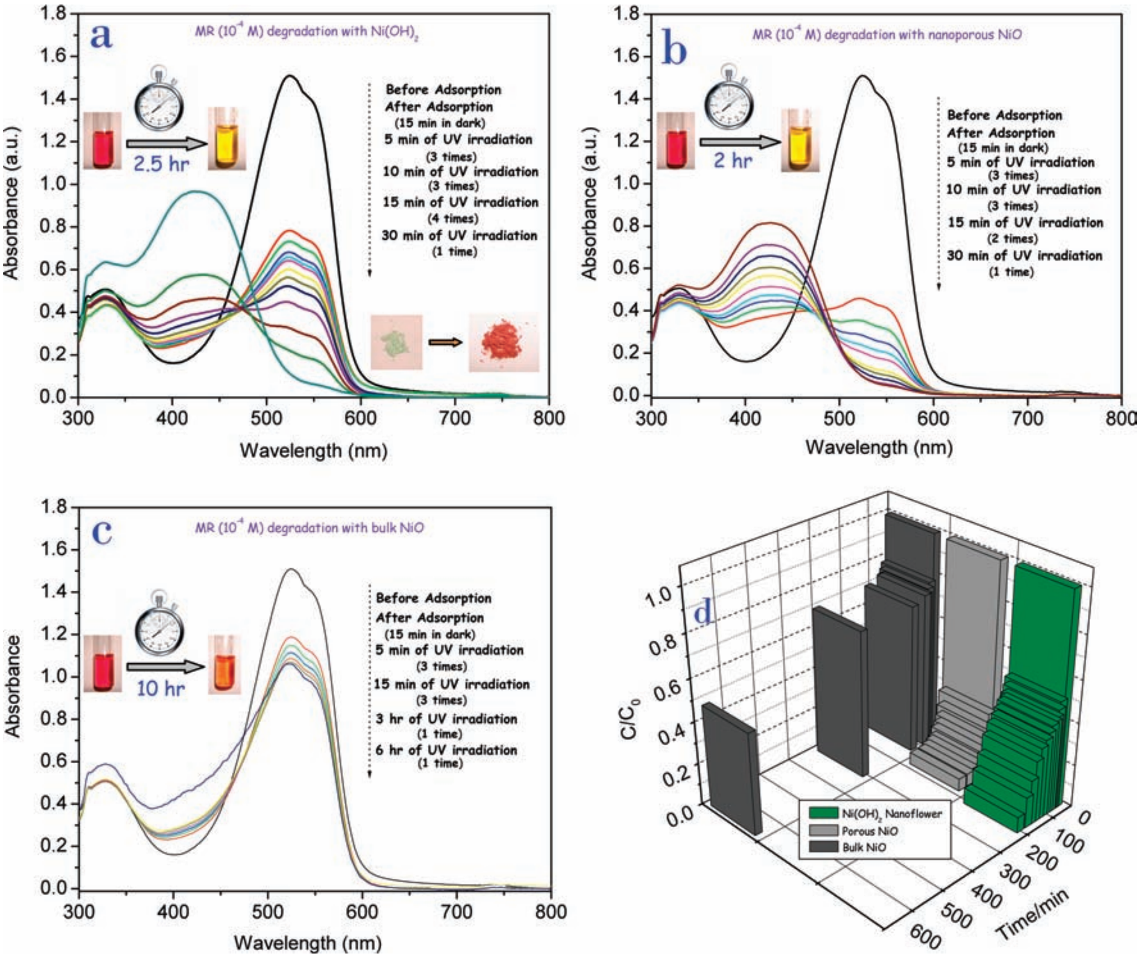

**Figure 9.** UV−visible spectra of the time-dependent degradation of methyl red (MR) under UV irradiation with (a) synthesized Ni(OH)$_2$ nanoflower, (b) nanoporous NiO, and (c) bulk NiO. Digital photographs present the color change upon degradation. (d) Comparative bar-diagrammatic representation of the first-order reaction kinetics with the above materials [conditions: [MR] = 10$^{-4}$ M; radiating source, a 15 W Philips medium-pressure mercury lamp ($\lambda$ = 365 nm)].

mainly silver, gold, and copper,[42] and a few transition metals (Ni, Pd, Pt, Co, Fe, Ga, etc.),[43] as many people had anticipated, in some quarters, semiconductor nanoparticles have also been observed to contribute in SERS with a typical enhancement factor of $10^1-10^3$. From this perspective, Lombardi's group has made an assortment of significant contributions to embellish the pathway of obtaining SERS from the so-called "ill-defined" semiconductor substrates.[44]

Encouraged by the puffy structures of the flowery $\beta$-Ni(OH)$_2$, a secondary material could easily be deposited within the framework to result in the formation of a functional composite material,[45] and taking this structural advantage, we have introduced silver nanoparticles within the inorganic matrix and the material Ag@Ni(OH)$_2$ has been addressed as a pertinent candidate for greeting SERS from suitable nearby molecules located on (or within) the latter material. The hybrid material bears a similar morphology, only differentiating in the thickness aspect, where we could notice a relative fatty nature of the petals, and this is the possible outcome of the deposition of in situ produced silver nanoparticles (Figure S9 in the Supporting Information). The derivative material has been further characterized by XRD and EDX analysis to show the presence of the secondary materials (Ag) beyond a doubt (Figure S10 in the Supporting Information).

Here the study presents the SERS spectrum of 4-mercaptopyridine (4-MP) from the nanocomposite, and their characteristic manifestation prescribes more diagnostic features related to the composite−analyte interaction. Table S1 in the Supporting Information summarizes the frequencies and

---

[42] (a) Roca, M.; Haes, A. J. *J. Am. Chem. Soc.* **2008**, *130*, 14273. (b) Aroca, R. F.; Constantino, C. J. L. *Langmuir* **2000**, *16*, 5425. (c) Vlckova, B.; Matejka, P.; van Outersterp, J. W. M.; Snoeck, T. L.; Stufkens, D. J. *Inorg. Chem.* **1994**, *33*, 2132. (d) Pagliai, M.; Muniz-Miranda, M.; Cardini, G.; Schettino, V. *J. Phys. Chem. A* **2009**, *113*, 15198.

[43] (a) Van Duyne, R. P.; Haushalter, J. P. *J. Phys. Chem.* **1983**, *87*, 2999. (b) Zou, S. Z.; Williams, C. T.; Chen, E. K. Y.; Weaver, M. J. *J. Am. Chem. Soc.* **1998**, *120*, 3811. (c) Wu, P. C.; Khoury, C. G.; Kim, T.-H.; Yang, Y.; Losurdo, M.; Bianco, G. V.; Vo-Dinh, T.; Brown, A. S.; Everitt, H. O. *J. Am. Chem. Soc.* **2009**, *131*, 12032. (d) Mengoli, G.; Musiani, M. M.; Fleischmann, M.; Mao, B.; Tian, Z. Q. *Electrochim. Acta* **1987**, *32*, 1239. (e) Yamada, H.; Yamamoto, Y. *Chem. Phys. Lett.* **1981**, *77*, 520. (f) Bilmes, S. A.; Rubim, J. C.; Otto, A.; Arvia, A. J. *Chem. Phys. Lett.* **1989**, *159*, 89. (g) Ren, B.; Huang, Q. J.; Cai, W. B.; Mao, B. W.; Liu, F. M.; Tian, Z. Q. *J. Electroanal. Chem.* **1996**, *415*, 175. (h) Sarkar, S.; Pande, S.; Jana, S.; Sinha, A. K.; Pradhan, M.; Basu, M.; Saha, S.; Yusuf, S. M.; Pal, T. *J. Phys. Chem. C* **2009**, *113*, 6022. (i) Sarkar, S.; Pradhan, M.; Sinha, A. K.; Basu, M.; Pal, T. *J. Phys. Chem. Lett.* **2010**, *1*, 439.

[44] (a) Sun, Z. H.; Wang, C. X.; Yang, J. X.; Zhao, B.; Lombardi, J. R. *J. Phys. Chem. C* **2008**, *112*, 6093. (b) Sun, Z. H.; Zhao, B.; Lombardi, J. R. *Appl. Phys. Lett.* **2007**, *91*, 221106. (c) Yang, L. B.; Jiang, X.; Ruan, W. D.; Zhao, B.; Xu, W. Q.; Lombardi, J. R. *J. Phys. Chem. C* **2008**, *112*, 20095. (d) Richter, A. P.; Lombardi, J. R.; Zhao, B. *J. Phys. Chem. C* **2010**, *114*, 1610.

[45] Zhang, S.; Zeng, H. C. *Chem. Mater.* **2009**, *21*, 871.

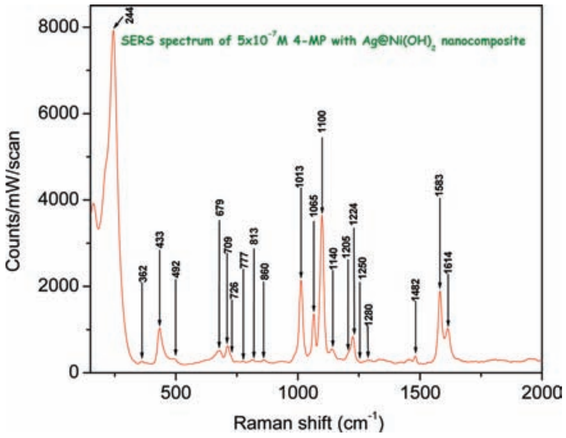

**Figure 10.** SERS spectrum of 4-MP from a Ag@Ni(OH)$_2$ nanocomposite [conditions: [4-MP] = $5 \times 10^{-7}$ M; excitation source, He−Ne laser emitting at a wavelength of 632.8 nm].

vibrational assignments of Raman bands of 4-MP. As we can see from Figure 10, the NRS spectrum of solid 4-MP significantly differs from the SERS spectrum in vibrational figures of merit. Noticeable changes are observed in the frequencies. The spectral analysis is presented in the Supporting Information.

To evaluate the limit of detection of 4-MP by employing this analytical tool by the composite, we have extended our study with its further lower concentration where we could observe the competence of the material to detect the concentration down to a nanomolar level (Figure S11 in the Supporting Information). The enhanced vibrational modes at ~1387 and ~1142 cm$^{-1}$ ($b_2$ vibrational modes) compared to that of only silver nanoparticles imply an improved metal-to-ligand charge transfer for the material.

The general consensus attributes the observed enhancement to contributions from two mechanisms: a long-range electromagnetic (EM) effect and a short-range chemical (CHEM) effect, although for the semiconductor particles because they often have plasmon resonance far from the excitation wavelength used, here these SERS spectra are dominated by a charge-transfer (CT) mechanism. The reality of this proposal is readily verified with the blue shifting of the bands at ~1595 and ~1089 cm$^{-1}$ of pure 4-MP to ~1583 and ~1065 cm$^{-1}$, respectively, in the SERS spectrum (Figure 10). This information authenticates that CT operates from the conduction band of the deposited silver nanoparticles to the $\pi$* level (LUMO) of the adsorbed molecule. In a true sense, the CHEM and EM mechanisms collectively contribute to the SERS enhancement and are not readily separable.[46] Any theoretical approach that challenges their separation will probably fail in one or more limits. Also, the "Schottky barrier", a dipolar layer juxtaposed between the metal deposited and the semiconductor, may have a bearing on the said SERS enhancement.[47]

## Conclusions

In summary, a trouble-free and simple ammonothermal methodology has been accepted as a straightforward protocol for the exploitation of highly anisotropic Ni(OH)$_2$ nanostructures. Of special interest is the explicit regulation in structural arrangements of the hydroxide material with a simple manipulation in the ammonia concentration and reaction time. Both parameters play a major role in the reaction dynamics. Ni(OH)$_2$ is observed to crystallize in the $\beta$ phase with a brucite structure and form a flowerlike morphology built up with plentiful patterned and aligned nanopetals. A conformational change from flower to truncated triangular stacked nanoplates to finally hexagonally stacked nanoplates with columnar morphology is exclusively achievable with an increase in the NH$_3$ concentration with an explanation from the surface coverage, hydrogen bonding, and surface energy. Microporous and mesoporous behaviors of the different nanostructures have been ascertained by BET gas sorption measurements. Following the whole evaluation process, we are inclined to illustrate the patterning of the Ni(OH)$_2$ textures involving a sequence of dissolution, recrystallization, and oriented attachment. Ultimately, the UV-activated photocatalytic property of the material has been bestowed with complete mineralization of an organic dye molecule and also provides an opportunity to make a secondary functional material with embedded silver nanoparticles, and the derived composite gives rise a more refined description of the SERS activity with 4-MP in its low concentration level. Thus, in the approach with the advantages of inexpensive experimental setup and simple and greener synthetic routes, the impressive increase in the variety of particle shapes promises to be transformed into a proliferation of revolutionary structures and materials that may readily be scaled up for industrial production.

**Acknowledgment.** The authors are thankful to the CSIR, UGC, and DST (New Delhi, India) and Indian Institute of Technology, Kharagpur, for financial assistance.

**Supporting Information Available:** TEM and HRTEM images on a different sides of the nanopetals, Raman spectrum of the sample with analysis and a schematic presentation of the Raman-active modes, magnetic property of the sample with corresponding magnetization plots, TEM and HRTEM analyses of hexagonal columnar structures, BET isotherms with pore-size distribution and an analysis for hexagonally stacked nanocolumns, FTIR spectrum of the $\beta$-Ni(OH)$_2$ hexagonal nanocolumn, FESEM images of Ni(OH)$_2$ synthesized with hexamethylenetetramine and pyridine, FESEM images of a Ag@Ni(OH)$_2$ nanocomposite with its characterized XRD and EDX patterns, analytical explanation of the SERS spectrum, the SERS spectrum of 4-MP at the nanomolar level of concentration over a Ag nanoparticle and the nanocomposite material, and Table S1 describing frequencies and vibrational assignments of Raman bands of 4-MP. This material is available free of charge via the Internet at http://pubs.acs.org.

---

(46) (a) Schatz, G. C. *Acc. Chem. Res.* **1984**, *17*, 370. (b) Sarkar, S.; Pande, S.; Jana, S.; Sinha, A. K.; Pradhan, M.; Basu, M.; Chowdhury, J.; Pal, T. *J. Phys. Chem. C* **2008**, *112*, 17862.

(47) (a) Kraya, R.; Kraya, L. Y.; Bonnell, D. A. *Nano Lett.* **2010**, *10*, 1224. (b) Tejedor, C.; Flores, F.; Louis, E. *J. Phys. C: Solid State Phys.* **1977**, *10*, 2163. (c) Louie, S. G.; Chelikowsky, J. R.; Cohen, M. L. *Phys. Rev. B* **1977**, *15*, 2154.